Ultralow Switching-Current Density in All-Amorphous W-Hf/Co-Fe-B/TaO_x Films

K. Fritz,[1,*] L. Neumann,[2] and M. Meinert[3,†]

[1] *Center for Spinelectronic Materials and Devices, Department of Physics, Bielefeld University, Bielefeld D-33501, Germany*

[2] *Argelander Institute for Astronomy, Department of Physics, Bonn University, Bonn D-53121, Germany*

[3] *Department of Electrical Engineering and Information Technology, Technical University of Darmstadt, Merckstraße 25, Darmstadt D-64283, Germany*

(Received 6 November 2019; revised 13 July 2020; accepted 13 July 2020; published 17 September 2020)

We study current-induced deterministic magnetization switching and domain-wall motion via polar Kerr microscopy in all-amorphous $W_{66}Hf_{34}$/Co-Fe-B (CFB)/TaO_x with perpendicular magnetic anisotropy and a large spin Hall angle. Investigations of magnetization switching as a function of the in-plane assist field and the current-pulse width yield switching-current densities as low as 3×10^9 A/m^2. We accredit this low switching-current density to a low depinning-current density, which is obtained from measurements of domain-wall displacements upon current injection. This correlation is verified by investigations of a Ta/CFB/MgO/Ta reference sample, which shows critical-current densities that are at least one order of magnitude larger.

DOI: 10.1103/PhysRevApplied.14.034047

I. INTRODUCTION

Switching of ferromagnetic thin films by means of the spin Hall effect (SHE) in heavy metal/ferromagnetic (HM/FM) bilayers with perpendicular magnetic anisotropy (PMA) has been studied intensively over recent years [1–15]. In these systems, the switching-current density j_{sw} is typically in the order of 10^{10} to 10^{11} A/m^2. Recent work suggests that the SHE switching is limited by the depinning of domain walls [16]. Therefore, a decrease of the depinning-current density j_{dep} should result in a reduced j_{sw}. Micromagnetic simulations [17] show that the pinning of domain walls depends on the ratio of the domain-wall width $\pi\Delta_{DW}$ to the average grain size $\langle L\rangle$, where the maximum pinning strength is found for $\pi\Delta_{DW} \approx \langle L\rangle$. For sufficiently small grains ($\langle L\rangle \ll \pi\Delta_{DW}$), local variations of the anisotropy, which give rise to pinning, are averaged out over the domain-wall width, resulting in weak pinning. Pinning is thus minimized in single-crystal films with $\langle L\rangle \gg \pi\Delta_{DW}$ or in nanocrystalline or amorphous films with $\langle L\rangle \ll \pi\Delta_{DW}$. This hypothesis is supported by a report on reduced pinning in nanocrystalline W/Co-Fe-B (CFB)/MgO thin films, prepared via sputter deposition at high deposition rates [18], and a similar observation of weak pinning of skyrmions [19]. Based on this hypothesis, in the present work we investigate the switching current densities in an all-amorphous system and study its relation to domain-wall pinning. For this purpose, we continue our investigations of a W_xHf_{x-1} 8 nm / CFB 3 nm / TaO_x 2 nm system [20], which exhibits a phase transition from a segregated phase mixture to an amorphous alloy for $x \leq 0.7$. Due to the accompanying jump in resistivity, the spin Hall angle (SHA) shows a pronounced maximum of $\theta_{SH} = -0.2$ at the phase transition. For the amorphous compositions, x-ray diffraction (XRD) patterns indicate at most some local order with a coherent scattering length of $D_z \approx (0.9 \pm 0.2)$ nm. In this system, PMA can be obtained by decreasing the FM-layer thickness and postannealing the sample. First observations of domain nucleation and expansion upon out-of-plane field application show the formation of large domains with only a few pinning sites. We understand this as a hint for weak pinning in the amorphous W-Hf, making this system interesting for investigation of a correlation between the lack of crystallinity and weak pinning. Finally, the large SHA of the amorphous W-Hf should allow for efficient current-induced magnetization switching.

Here, we report on current-induced magnetization switching experiments (CIMS) and current-induced domain-wall motion (CIDWM) experiments, performed on all-amorphous $W_{66}Hf_{34}$/CFB/TaO_x with perpendicular magnetic anisotropy and a large SHA via polar Kerr microscopy. For comparison, we additionally

*kfritz@physik.uni-bielefeld.de
†markus.meinert@tu-darmstadt.de

investigate a reference system consisting of Ta/CFB/MgO/Ta, which is known to exhibit stronger domain-wall pinning. After preparation via sputter deposition, both systems are electrically and magnetically characterized to ensure comparability and patterned for the observation of domain-wall motion and magnetization switching. In case of the W-Hf/CFB/TaO_x, the maintenance of the amorphous phase during the sample processing is verified by comparing the sheet resistance before and after postannealing. In order to study the correlation between the switching current density and the depinning-current density, we conduct the same CIMS and CIMDW experiments on both systems. We obtain critical current densities that are at least one order of magnitude lower for the W-Hf system, respectively. To support our conclusion that a reduced depinning-current density will result in a reduced switching-current density, we evaluate the influence of Joule heating and the energy barriers for nucleation and depinning of domains in both systems. Additionally, we perform measurements of the spin Hall effective fields in various configurations via harmonic response analysis to ensure that the difference in the critical-current densities is not a result of significantly different spin-orbit torque (SOT) efficiencies.

II. METHODS

A. Sample preparation

The thin films are grown in UHV magnetron (co)sputtering systems at room temperature on thermally oxidized Si wafers and postannealed in a vacuum furnace with a pressure lower than 5×10^{-7} mbar. W-Hf thin films are prepared via cosputtering. The thermal stability of the amorphous phase is verified by comparing the sheet resistance, measured via a four-probe technique, before and after annealing. A nominal tungsten content of 66% is chosen for further investigations. All layers in this sample are deposited with an Ar working pressure of 2×10^{-3} mbar. Perpendicular magnetic anisotropy (PMA) is obtained with a thin CFB layer and by postannealing the sample at 180 °C for 20 min. The full stack is Si(001)/SiO_x 50 nm / $W_{66}Hf_{34}$ 8 nm / $Co_{40}Fe_{40}B_{20}$ 0.85 nm / TaO_x 2.55 nm / SiN 1.5 nm. For comparison, a reference sample consisting of Si(001)/SiO_x 50 nm / Ta 8 nm / $Co_{40}Fe_{40}B_{20}$ 1.1 nm / MgO 1.8 nm / Ta 1.5 nm is prepared. The Ar working pressure during the sputter deposition is 1.2×10^{-3} and, for the MgO layer, 2.2×10^{-2} mbar. Here, MgO allows for PMA with a thicker CFB layer. Longitudinal and polar magneto-optical Kerr effect (MOKE) measurements at room temperature are performed to characterize the magnetization of the samples. In order to ensure comparability of the two systems, the anisotropy that determines the domain-wall width is set to a similar value. Therefore, the reference sample is postannealed for 20 min at 280 °C to match the anisotropy of the W-Hf system. Maintenance of the amorphous CFB during the annealing is, again, verified by measurements of the sheet resistance. Additionally, the crystallinity of the samples is investigated via XRD with Cu K_α radiation in a diffractometer with Bragg-Bretano geometry. The measurements are performed with a sample offset to attenuate substrate peaks and clearly assign any measured peaks to the thin films. The saturation magnetization M_s is determined via vibrating-sample magnetometry (VSM).

The samples are patterned via electron-beam lithography and ion-beam milling into line bars and Hall bars and Ta/Au contact pads are subsequently deposited via sputter deposition. The line bars, with geometries of 50×6 μm^2 and 100×2 μm^2, are used for observation of the domain dynamics and switching upon current injection. The Hall bars, consisting of 40×3 μm^2 and 30×3 μm^2 bars with contact lines, are used to determine the SOT efficiencies ξ.

B. Observation of domain-wall motion and magnetization switching

CIMS is observed with a home-built Kerr microscope utilizing the polar MOKE [21,22], using a commercial Carl Zeiss metallurgical microscope. While simultaneously applying current pulses and static in-plane magnetic fields ($B_{max} = 400$ mT) parallel to the line bars, the brightness of the Kerr image is measured as a function of the applied current density. From the resulting hysteresis loops [cf. Fig. 5(a)], j_{sw} is obtained as a function of the pulse width τ and the longitudinal field B_x. The final j_{sw} is calculated as a weighted mean from at least three individual measurements. For more detailed information about the error analysis and statistics, see to our previous work [20].

CIDWM is observed in differential Kerr images. The differential images are stabilized in software via frame cropping and FFT-based image registration [23]. Noise reduction is achieved with a convolutional neural network (FFDNet) [24,25] running in real time on a graphics processing unit. The domain-wall velocity v_{DW} is obtained from the displacement of a domain wall divided by the number of pulses N and τ as a function of the applied current density. In multipulse experiments ($N > 1$), the pulse on:off ratio is chosen small enough to ensure full cool-down of the line between pulses.

C. Harmonic response analysis

The motion and expansion of domain walls is caused by dampinglike (DL) and fieldlike (FL) effective fields $B_{DL/FL}$, which originate from the SHE due to an in-plane current injection. A measure to compare these fields is the SOT efficiency

$$\xi_{DL/FL} = \frac{2e}{\hbar} \frac{M_s t_{FM} B_{DL/FL}}{j_0} c_{AR}. \quad (1)$$

The DL and FL effective fields are obtained from harmonic Hall voltage measurements. All measurements are conducted by injecting an in-plane ac current $I(t) = I_0 \sin(\omega t)$ into the Hall bars and simultaneously recording the in-phase first-harmonic and out-of-phase second-harmonic Hall voltages using a Zurich Instruments MFLI multidemodulator lock-in amplifier. From the resulting effective fields and the current density amplitude j_0, the presented SOT efficiencies $\xi_{DL/FL}$ are determined as a weighted mean from multiple measurements, taking into account the aspect ratio of the Hall bars with a correction factor c_{AR}[26]. Because of the similar resistivities of all conducting layers (about 180–200 $\mu\Omega$ cm), no correction within a parallel resistor model has to be applied. However, we take into account the different orientations of the magnetic moments in both the domains and the domain walls. In the latter case, even though the sample has PMA, the moments lie in the film plane and the resulting effective fields are not necessarily the same as for the out-of-plane-oriented magnetic moments. To separate and compare the effective fields, we conduct the measurements in two geometries of the external magnetic field, which is applied during the measurements.

For the determination of the effective fields with out-of-plane geometry, representing the magnetic moments in the domains, a measurement scheme as described by Hayashi *et al.* [27] is useful. Following this scheme, the SOT fields

$$B_{x/y} = -2\frac{\left(b_{x/y} \pm 2\chi b_{y/x}\right)}{1 - 4\chi^2} \tag{2}$$

are determined. The sign $\pm$ denotes the orientation of $\vec{M}$ along $\pm z$ and $\chi = R_P/R_A$ is the ratio of the planar and anomalous Hall resistances, which are obtained from in-plane field rotation and out-of-plane field sweeps, respectively. $b_{x/y} \equiv \left[\left(\partial V_{2\omega}/\partial H\right) / \left(\partial^2 V_\omega/\partial H^2\right)\right]$ are extracted from in-plane field sweeps longitudinal (x) and transverse (y) to the Hall bars, where the x direction corresponds to the DL and the y direction to the FL effective field. The field sweeps are performed in a vector magnet consisting of two coil pairs oriented along the x and y directions and a maximum in-plane field of 0.3 T.

An in-plane measurement scheme identical to that used in our previous work [20] is applied to obtain the effective fields that cause torques in the domain walls. Here, a dual-Halbach-cylinder array with a rotating magnetic field up to $B_{ext} = 1.0$ T (MultiMag, Magnetic Solutions Ltd.) is used for in-plane field rotation. The scheme is facilitated by the weak PMA in our samples. The current-induced effective SOT-field amplitudes B_{DL} and B_{FL}, associated with the DL and FL SOTs, are derived from the rms value of the second-harmonic Hall voltage:

$$V_{2\omega} = \left(-\frac{B_{FL}}{B_{ext}} R_P \cos 2\varphi - \frac{1}{2}\frac{B_{DL}}{B_{eff}} R_A + \alpha' I_0\right) I_{rms} \cos\varphi. \tag{3}$$

The DL effective fields and the anomalous-Nernst contribution $\alpha' I_0$ are separated by their dependence on the external field (for a detailed discussion of the method, see Ref. [20]). Here, φ is the in-plane field angle with respect to the current direction and $B_{eff} = -B_{ani} + B_{ext}$ is the effective magnetic field. We use the convention $B_{ani} > 0$ for spontaneous PMA.

III. RESULTS AND DISCUSSION

In our previous work [20], we have reported on a large SHE in W-Hf/CFB/TaO_x/SiN films, observed as a result of the formation of an amorphous phase for a tungsten content below 70%. Due to the accompanying jump in resistivity, the SHA shows a pronounced maximum of $\theta_{SH} = -0.2$ at the phase transition. This stoichiometry, however, shows a decrease in resistivity upon postannealing, indicating crystallization. In order to find a thermally stable amorphous composition with a SHA that is as large as possible, W-Hf thin films with a nominal tungsten content of 62%–68% are prepared. Thermal stability is verified in all samples and the measured high resistivities confirm equivalence to our previous work. To compensate for slight process instabilities during the deposition, a tungsten content of 66% is chosen for further investigations. Due to the usage of TaO_x instead of MgO, which is known to crystallize upon annealing, we assume that we can maintain the all-amorphous character of our sample stack throughout the sample processing. The final film stack has an effective resistivity of $\rho_{xx} = 185$ $\mu\Omega$ cm and a magnetization of $M_s = 684$ kA/m. The low magnetization indicates the presence of a magnetic dead layer in the CFB, probably due to oxidation during the formation of the TaO_x layer. The XRD pattern of the annealed sample stack, shown in Fig. 1, shows no evidence for a crystal structure or an atomic local order, indicating an all-amorphous system. From the MOKE measurements, presented in Figs. 2(a) and 2(b), an anisotropy field of $B_{ani} = 123$ mT and a very low coercive field of $B_c \approx 80$ μT are determined. The latter allows for nucleation and expansion of domains in the $W_{66}Hf_{34}$/CFB/TaO_x/SiN film with low out-of-plane field pulses, as shown in Fig. 3 for field pulses with $B_z = 100$ μT and $\tau = 0.1$ s. The resulting domain only contains a few macroscopically visible pinning sites, highlighted as exemplary cases, using red arrows, in image 8 of Fig. 3. Here, the initial magnetic orientation is pinned and causes the riverlike structures in the radially expanding opposing white domain. From measurements of the growth of the domain after each field pulse, we estimate a domain-wall

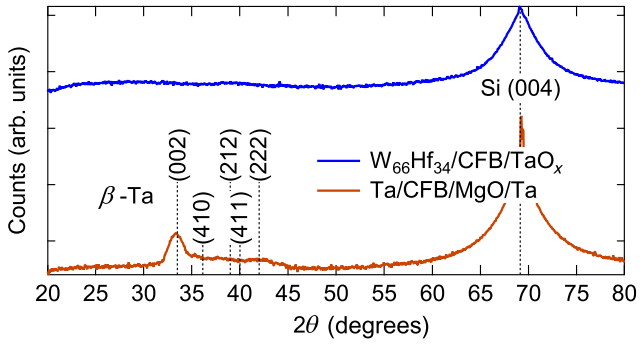

FIG. 1. The XRD pattern of the annealed $W_{66}Hf_{34}$/CFB/TaO_x and Ta/CFB/MgO/Ta sample stacks. The Si (004) peak is attenuated by up to 400 times with respect to the specular geometry. The (forbidden) Si (002) peak is suppressed below the noise level of the measurement.

velocity of $v_{DW} \approx 0.23$ mm/s, which corresponds to the creep regime, as is discussed further below. An analysis with the ImageJ software plugin Delaunay Voronoi yields a pinning-site mean distance of $\bar{d} = (144.5 \pm 68.5)$ μm.

The Ta/CFB/MgO/Ta reference sample is postannealed to match the anisotropy of the $W_{66}Hf_{34}$ sample, resulting in $B_{ani} = 120$ mT and $B_c = 3$ mT, determined from the MOKE measurements shown in Figs. 2(c) and 2(d). The final sample stack has an effective resistivity of $\rho_{xx} \approx 180$ $\mu\Omega$ cm and a saturation magnetization of $M_s = 1088$ kA/m. From the XRD pattern in Fig. 1, we infer the formation of β-Ta in this sample, which is in good agreement with its large resistivity [28]. The prominent peak at $2\theta = 33.35°$, which corresponds to the β-Ta (002), allows for determination of a minimum length of coherent scattering $D_z \approx 6$ nm via Scherrer's formula. The broad shoulder

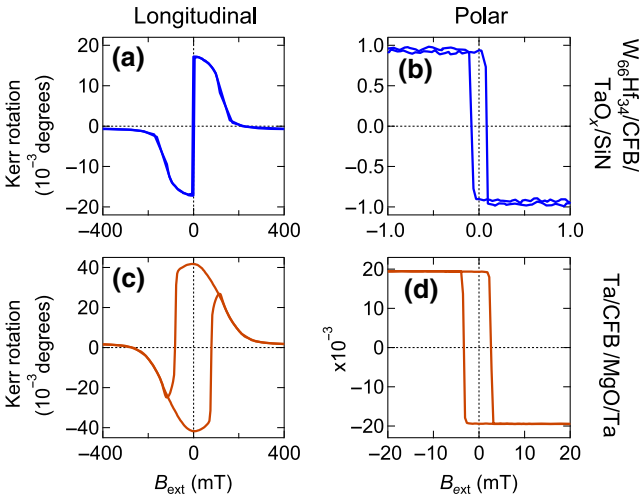

FIG. 2. The longitudinal and polar MOKE measurements of the final (a),(b) $W_{66}Hf_{34}$/CFB/TaO_x/SiN and (c),(d) Ta/CFB/MgO/Ta sample stacks.

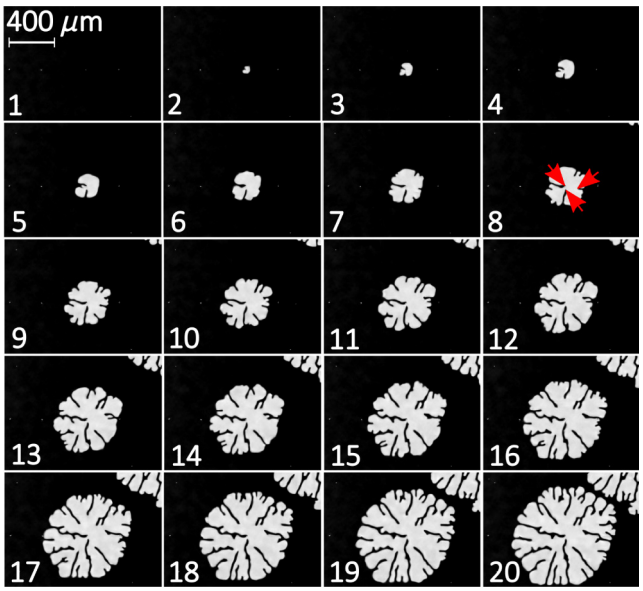

FIG. 3. Differential Kerr images of an opposing domain nucleated and expanded by out-of-plane field pulses in a $W_{66}Hf_{34}$/CFB/TaO_x/SiN film with $v_{DW} \approx 0.23$ mm/s. Each image is recorded after application of a single pulse with $B_z = 100$ μT and $\tau = 0.1$ s. The red arrows in image 8 mark exemplary pinning sites.

next to this peak could be caused by various other scattering planes of the β-Ta, some of which are marked in Fig. 1. In comparison to the $W_{66}Hf_{34}$ sample, here the application of out-of-plane field pulses results in the nucleation of many opposing domains with much narrower and denser riverlike structures, as shown in Fig. 4. In the interest of comparability, the domain growth is observed with the same magnification and domain-wall velocity of $v_{DW} \approx 0.23$ mm/s, which is achieved with single pulses

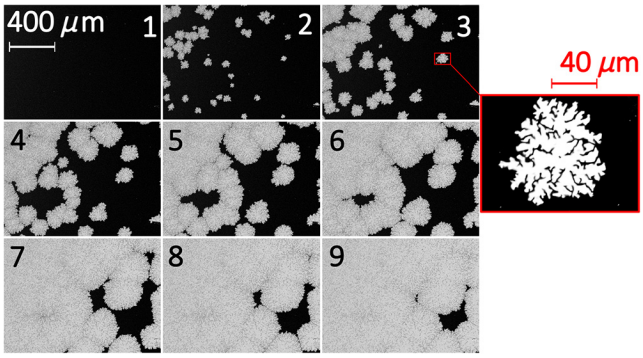

FIG. 4. Differential Kerr images of opposing domains nucleated and expanded by out-of-plane field pulses in a Ta/CFB/MgO/Ta film with $v_{DW} \approx 0.23$ mm/s, each recorded after application of a single pulse with $B_z = 2.7$ mT and $\tau = 0.1$ s. The red-framed inset shows a domain nucleated at the marked area with the same field-pulse parameters, observed with higher magnification.

of $B_z = 2.7$ mT and $\tau = 0.1$ s. From the Delaunay triangulation, we obtain a mean distance $\bar{d} = (9.6 \pm 5.0)\ \mu$m between the pinning sites.

In Fig. 5(a), we show hysteresis loops obtained by observing CIMS in the $50 \times 6\ \mu m^2$ line bars with varying in-plane longitudinal fields in the all-amorphous $W_{66}Hf_{34}$-based sample. Each data point is recorded after $N = 20$ pulses with a pulse width $\tau = 1 \times 10^{-3}$ s. Analogously, CIMS experiments are conducted with different pulse widths and the resulting j_{sw} is displayed in Fig. 5(b) as a function of τ for varying in-plane fields. We observe a decrease of j_{sw} for an increasing pulse width and longitudinal field, with ultralow switching-current densities in the range of $3 \times 10^9 < j_{sw} < 2.8 \times 10^{10}$ A/m^2. These are the lowest switching-current densities reported so far in HM/FM bilayer systems and a similarly low switching-current density has only been found in an epitaxial system

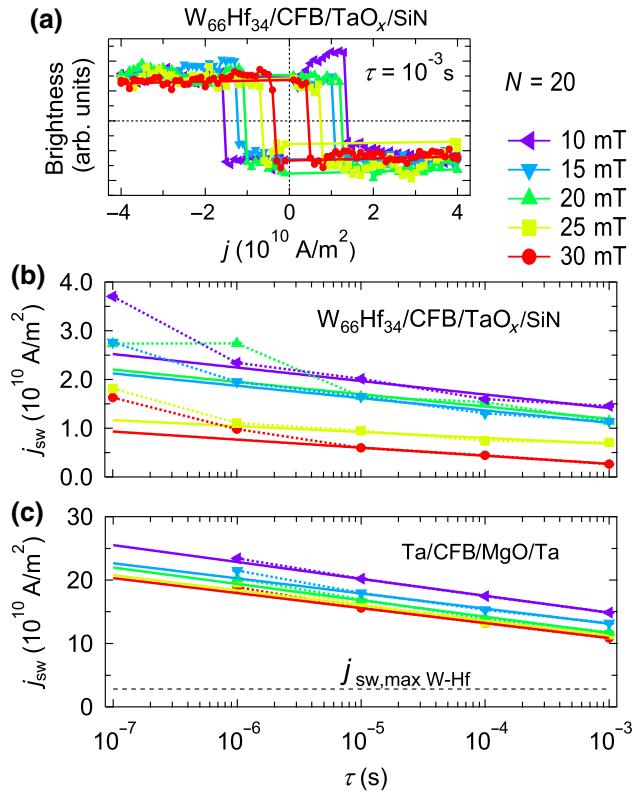

FIG. 5. (a) Hysteresis loops recorded via Kerr microscopy, showing the Kerr-image brightness as a function of the applied current density for different in-plane fields B_x. Each data point is recorded after pulsing $N = 20$ times with a pulse width of $\tau = 1 \times 10^{-3}$ s. The switching-current density in $50 \times 6\ \mu m^2$ (b) $W_{66}Hf_{34}/CFB/TaO_x/SiN$ and (c) Ta/CFB/MgO/Ta line bars as a function of the pulse width for different in-plane fields obtained from the hysteresis loops. Data for $\tau = 10^{-7}$ s are missing for Ta, because an amplifier with impedance mismatch is used that distorts the short pulses. The solid lines show fits of Eq. (5) to the experimental data.

[29]. The same experiment is performed using the Ta reference sample. The resulting j_{sw}, presented in Fig. 5(c), again shows a decrease with an increasing field and pulse width and matches the results from other reports [11,16], found for similar layer stacks. However, with $1.2 \times 10^{11} < j_{sw} < 3.0 \times 10^{11}$ A/m^2, the switching-current density of the Ta reference is up to 40 times larger than in the amorphous $W_{66}Hf_{34}$ sample.

In order to rule out excessive Joule heating as a reason for the ultralow switching-current densities in the $W_{66}Hf_{34}$ sample, we calculate the temperature rise ΔT in the line bars. We use a two-dimensional model as derived by You *et al.* [30], to obtain the maximum temperature rise at the end of a current pulse ($t = \tau$):

$$\Delta T(t) = c\frac{whj^2}{\pi\kappa_S\sigma}\left[\operatorname{arcsinh}\left(\frac{2\sqrt{\mu_S t}}{\alpha w}\right) - \theta\,(t-\tau)\operatorname{arcsinh}\left(\frac{2\sqrt{\mu_S\,(t-\tau)}}{\alpha w}\right)\right]. \quad (4)$$

Here, κ_s and μ_s are the heat conductivity and the thermal diffusivity of the Si substrate and c is a temperature-scaling factor to take into account the 50-nm SiO_2 layer on top of the substrate. The latter is determined from finite-element-method (FEM) simulations to be $c \approx 1.45$. $\alpha = 0.5$ is chosen, as proposed by You *et al.* As both samples are comparable in terms of film thickness and resistivity, we estimate ΔT using $h = 9$ nm, $\rho = 1/\sigma = 180\ \mu\Omega$ cm, and $w = 6\ \mu$m as a function of τ and j, presented in Fig. 6 on a logarithmic scale. The inset shows $\Delta T(t)$ for $j = 10^{11}$ A/m^2 and $\tau = 5 \times 10^{-6}$ s. The black and green markers highlight the ΔT in the $W_{66}Hf_{34}$ and Ta line bars corresponding to the switching-current densities found for $B_x = 10$ mT and the investigated pulse widths τ, respectively. The dashed line is the equitemperature line with $\Delta T = 1$ K as a guide to the eye. We find a maximum temperature rise of $\Delta T_{Ta} \approx 50$ K in the Ta line bars, while in the $W_{66}Hf_{34}$ the temperature rise does not exceed $\Delta T_{W\text{-}Hf} \approx 0.6$ K. Therefore, the Joule heating is low in the $W_{66}Hf_{34}$ and can be neglected. In the Ta line bars, on the other hand, the Joule heating is more prominent and we rather underestimate the switching-current densities here due to the additional thermal activation provided by the Joule heating. Next, we estimate the energy barrier $E_{B,0}$ for nucleation of an opposing domain. We start from the Néel-Arrhenius equation $\tau = \tau_0 \exp(E_B/k_BT)$ and assume a lowered energy barrier $E_B = E_{B,0}\left(1 - j_c/j_{c,0}\right)$ due to the effective fields that result from the current pulses. This leads to the following fit equation for the switching-current density [31]:

$$j_c = j_{c,0}\left[1 - \frac{k_BT}{E_{B,0}}\ln\left(\frac{\tau}{\tau_0}\right)\right]. \quad (5)$$

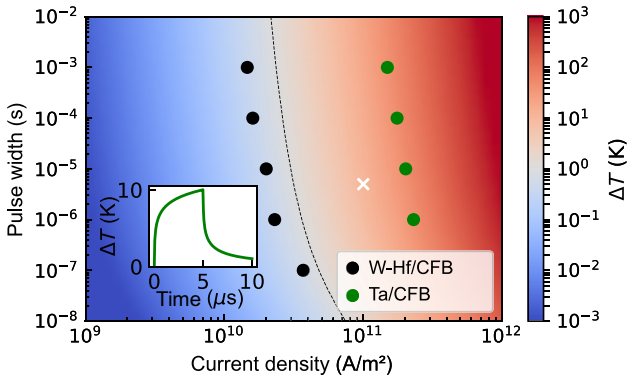

FIG. 6. The calculated temperature rise ΔT due to Joule heating as a function of the pulse width τ and current density j from a two-dimensional model [Eq. (4)] [30]. The markers highlight the ΔT corresponding to the switching-current densities obtained for the $W_{66}Hf_{34}$ and Ta sample with $B_x = 10$ mT and the investigated pulse widths τ, respectively. The dashed line marks $\Delta T = 1$ K. The inset shows the time dependence of ΔT for $j = 10^{11}$ A/m^2 and $\tau = 5 \times 10^{-6}$ s (white cross).

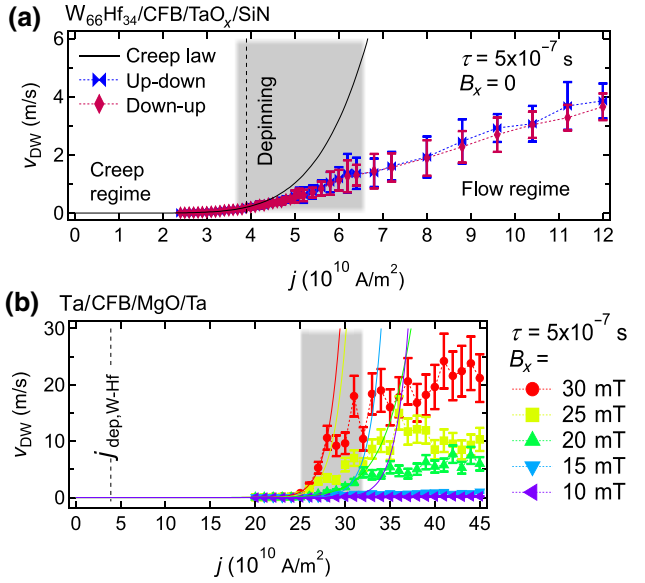

FIG. 7. The domain-wall velocity as a function of the current density in (a) $W_{66}Hf_{34}$/CFB/TaO_x/SiN and (b) Ta/CFB/MgO/Ta for different in-plane fields. The highlighted area marks the region of depinning.

For the attempt time τ_0, we assume $\tau_0 = 1$ ns. We obtain the fits that are presented as dashed lines in Figs. 5(b) and 5(c). For $B_x = 10$ mT, we find a nucleation energy barrier of $E_{B,0,\text{W-Hf}} \approx 0.65$ eV for the $W_{66}Hf_{34}$ sample and $E_{B,0,\text{Ta}} \approx 0.78$ eV for the Ta reference. The deviation for short pulses from Eq. (5) can be explained by slow domain-wall propagation: while the current density is large enough to nucleate an opposing domain, it is not large enough to drive the domain through the line bar, such that higher current density is needed to achieve full switching in the time given by the current pulses.

For a better understanding of the origin of the low switching-current density, we measure the velocity of the domain walls v_{DW} as a function of the driving force, which is the applied current density in our experiment. It can be generally divided into two regimes, the creep and the flow regime, separated by a region in which the depinning of the domain walls takes place [32–34]. In the flow regime, the velocity shows a linear dependence on the driving force, while in the creep regime, the motion of the domain walls is thermally activated and the velocity can be described by the creep law

$$v_{\text{DW}} = v_{\text{dep}} \exp\left\{-\frac{T_{\text{dep}}}{T}\left[\left(\frac{j}{j_{\text{dep}}}\right)^{-1/4} - 1\right]\right\}. \quad (6)$$

Here, j_{dep} denotes the depinning-current density and $T_{\text{dep}}/T = E_{\text{dep}}/k_B T = \Delta_{\text{dep}}$ corresponds to the thermal-stability factor of the system [35]. For the $W_{66}Hf_{34}$ sample, the measurements are performed in the 50×6 μm^2 line bars by applying current pulses with $\tau = 5 \times 10^{-7}$ s and a varying number N. CIDWM is observed for a zero-assist field, indicating that the domain walls are of a partial Néel-type due to the presence of the Dzyaloshinskii-Moriya interaction (DMI) [36]. Without an external magnetic field, the up-down and down-up domain walls move in the same direction, indicating that they have the same chirality. The motion of the up-down and down-up domain walls is analysed separately. The resulting domain-wall velocity for a zero-assist field, presented in Fig. 7(a), shows the expected change in slope in the gray-shaded area and, therefore, allows for a distinction between the creep and flow regimes. By fitting the creep law [Eq. (6)] to the data obtained for low current densities up to the gray-shaded area, we find a low depinning-current density of $j_{\text{dep}} = (3.9 \pm 0.3) \times 10^{10}$ A/m^2, marked with the dashed black line, and a thermal-stability factor of $\Delta_{\text{dep}} = 27 \pm 4$. We define the depinning-current density as the value j at which the creep law deviates from the measured data by at least one standard error. Interpolating the CIMS results in Fig. 5(b) to $\tau = 5 \times 10^{-7}$ s for $B_x = 10$ mT, we obtain the corresponding switching-current density $j_{\text{sw}} \approx 2.5 \times 10^{10}$ A/m^2, i.e., nearly identical to the depinning-current density for the same pulse width. We note that $B_x = 10$ mT is approximately the threshold value for observation of CIMS, which indicates that only for larger B_x is the homochirality of the up-down and down-up domain walls broken. This allows us to quantify the strength of the DMI from an individual analysis of v_{DW} for the up-down and down-up domain walls as a function of B_x [37,38]. A minimum of v_{DW} is expected for a particular B_x, where the sign of this field is opposite for the up-down and down-up domain walls (not shown). Here, the effective longitudinal

DMI field is exactly compensated, resulting in Bloch-type domain walls at one side of a domain and, therefore, vanishing B_{DL}. From the threshold field $B_x = B_{\mathrm{DMI}}$, the effective DMI constant,

$$D = B_{\mathrm{DMI}} M_s \Delta_{\mathrm{DW}}, \tag{7}$$

can be calculated [37,38]. Here, $\Delta_{\mathrm{DW}} = \sqrt{A/K_{\mathrm{eff}}}$ is the domain-wall width parameter, in which $A \approx 20$ pJ/m denotes the exchange constant [39] and $K_{\mathrm{eff}} = B_{\mathrm{ani}} M_s/2$ is the effective uniaxial anisotropy [38]. With a threshold value $B_x \approx 10$ mT $= B_{\mathrm{DMI}}$ and $\Delta_{\mathrm{DW}} \approx 22$ nm, a DMI constant of $D \approx 0.15$ mJ/m^2 is obtained.

For $j_{\mathrm{dep}} = 3.9 \times 10^{10}$ A/m^2 and $\tau = 5 \times 10^{-7}$ s, we find a depinning energy barrier of $E_{\mathrm{dep}} \approx 0.69$ eV, which is comparable to the corresponding energy barrier $E_{B,0} \approx 0.65$ eV for nucleation of an opposing domain. This result suggests that as soon as an opposing domain is nucleated, it can expand almost undisturbed in the line bar at the same current density. Observation of the CIMS process in the $W_{66}Hf_{34}$ line bars in the differential Kerr image supports this interpretation: as can be seen in Fig. 8, we find that the magnetization reversal happens via nucleation of a single domain, which then quickly expands upon the application of current pulses. Thus, the switching is dominated by the motion of the domain walls rather than by the nucleation process [40] and, therefore, just the domain-wall velocity is the limiting factor for CIMS.

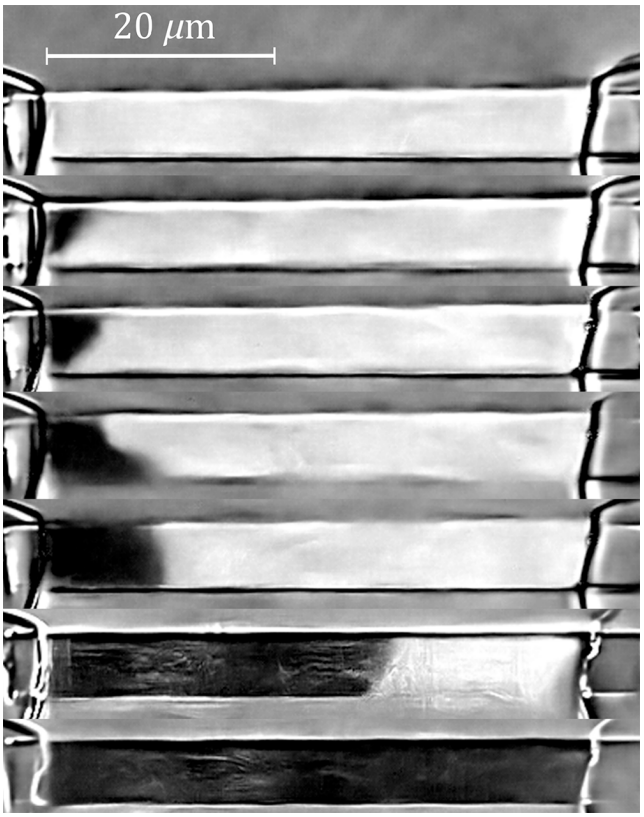

FIG. 8. Differential Kerr images depicting CIMS in $W_{66}Hf_{34}$/CFB/TaO_x/SiN. Single current pulses with $j = 2 \times 10^{10}$ A/m^2 and $\tau = 1 \times 10^{-4}$ s are applied with an in-plane field of $B_x = 20$ mT.

In the Ta reference sample, CIDWM is only observed under the application of longitudinal fields, indicating Bloch-type domain walls [36], where the magnetic moments in the domain walls are aligned parallel to the spin direction $\boldsymbol{\sigma}$ of the spin current. In order for a spin current to cause a DL field $\mathbf{B}_{\mathrm{DL}} = \boldsymbol{\sigma} \times \mathbf{m}$, the magnetic moments have to be tilted by an external field to have a magnetization component perpendicular to $\boldsymbol{\sigma}$. For this experiment, thinner and longer line bars have to be used to prevent nucleation of domain walls at the line edges due to the Oersted field and, on the other hand, to be able to observe the faster domain-wall propagation. The resulting domain-wall velocity, measured in line bars with a geometry of 100×2 μm^2 for different longitudinal fields and with $\tau = 5 \times 10^{-7}$ s, is presented in Fig. 7(b). Again, we observe a change in slope in the gray-shaded area.

Larger in-plane assist fields force the magnetization within the domain walls to be parallel to the applied current, resulting in a larger B_{DL} and higher DW velocities. The depinning-current density is obtained from fitting the creep law to the 10-mT measurement, as this field equals the DMI effective field of the $W_{66}Hf_{34}$ sample. We find that $j_{\mathrm{dep}} = (2.9 \pm 0.3) \times 10^{11}$ A/m^2, with a thermal-stability factor $\Delta_{\mathrm{dep}} = 105 \pm 7$. The switching-current density for comparable pulse parameters is obtained by extrapolation of the data in Fig. 5(c). For $B_x = 10$ mT, we obtain $j_{\mathrm{sw}} \approx 2.5 \times 10^{11}$ A/m^2, which is almost the same value as the depinning-current density. Using Eq. (4), we calculate the corresponding temperature rise of $\Delta T \approx 29$ K for the 100×2 μm^2 line bar and a resulting depinning energy barrier of $E_{\mathrm{dep}} \approx 2.9$ eV, which is considerably larger than the according nucleation barrier $E_{B,0} \approx 0.78$ eV. This suggests that, in contrast to the $W_{66}Hf_{34}$ sample, in the Ta reference sample, the switching is dominated by the nucleation of various domains and the pinning of the domain walls is the limiting factor for the switching. This conclusion is supported by observations of the nucleation process of opposing domains in both systems (Figs. 3 and 4).

A comparison of the results for both samples also emphasizes a direct correlation between j_{dep} and j_{sw}, as both current densities are of the same order of magnitude. Additionally to the lower depinning- and switching-current densities in the $W_{66}Hf_{34}$-based sample, we observe a significantly lower thermal-stability factor Δ_{dep}, which is in good agreement with earlier investigations of the correlation between the thermal stability and switching-current density in CIMS and CIDWM experiments with submicron stripes, where pinning results from edge effects [41].

Measurements of the DL and FL effective fields are performed in both samples to ensure that the significantly

lower switching- and depinning-current densities in $W_{66}Hf_{34}$ are not the result of a much larger SOT efficiency. For the Ta reference, we find identical SOT efficiencies for both in-plane and out-of-plane measurement schemes. Furthermore, the DL and FL values are very similar, incidentally, where the weighted mean is $\xi_{DL} \approx \xi_{FL} \approx -0.056 \pm 0.004$. In the $W_{66}Hf_{34}$ sample, the out-of-plane measurement scheme yields $\xi_{DL} \approx -0.138 \pm 0.063$ and $\xi_{FL} \approx -0.017 \pm 0.063$. From the in-plane configuration, we obtain $\xi_{DL} \approx -0.143 \pm 0.015$ and $\xi_{FL} \approx 0.092 \pm 0.034$. Again, the DL torques are very similar in both schemes, whereas the FL efficiencies are clearly different. The efficiency of the DL torque, which gives rise to the current-induced motion of the domain walls, is approximately 2.5 times larger in the $W_{66}Hf_{34}$-based sample. However, this is not sufficient to explain the factor of up to 40 between the switching- and depinning-current densities of the two sample types. The main difference between the samples is thus clearly the pinning strength, which is very weak in the $W_{66}Hf_{34}$-based sample.

IV. CONCLUSION

In summary, we investigate the current-induced magnetization switching in an all-amorphous $W_{66}Hf_{34}$/CFB/TaO_x sample stack, obtaining ultralow switching-current densities as low as 3×10^9 A/m^2. In order to understand the origin of this ultralow switching-current density, we evaluate various characteristics of the sample, some of which are summarized in Table I. Observation of the domain-wall motion reveals a depinning-current density of the same order of magnitude with a ratio of $j_{dep}/j_{sw} \approx 1.6$. A comparison with a Ta/CFB/MgO/Ta reference sample yields $j_{dep}/j_{sw} \approx 1.2$, emphasizing that this ratio is universally close to unity [41]. This result indicates a correlation between the switching- and depinning-current densities, where the switching is limited by the propagation of domain walls, rather than by their nucleation. We support this conclusion with an evaluation of the energy barriers for the nucleation and depinning $E_{B,0}$ and E_{dep} and observations of the nucleation and expansion of opposing domains in both systems. The latter reveals strongly differing domain structures with a mean distance of pinning sites $\bar{d}$ that is at least one order of magnitude larger in the $W_{66}Hf_{34}$-based sample. Based on the XRD pattern, we ascribe this reduced pinning to the lack of a crystal structure and, in particular, to the lack of grain boundaries and associated inhomogeneities of the magnetic parameters. The ultralow switching-current densities that we obtain for $W_{66}Hf_{34}$ therefore suggest that the all-amorphous character of the sample results in reduced pinning. This combination of a low pinning and the potentially large SHA in all-amorphous heavy metals, given by the intrinsic spin Hall effect due to the high resistivity, could be interesting for further investigations in the context of magnetization switching.

TABLE I. A comparison of the evaluated key points of both investigated systems: the length of coherent scattering D_z, the pinning-site mean distance $\bar{d}$, the switching- and depinning-current densities j_{sw} and j_{dep}, and the thermal-stability factor Δ_{dep}. For better conciseness, the values here are an estimation of the order of magnitude or are rounded.

	$W_{66}Hf_{34}$/CFB/TaO_x	Ta/CFB/MgO/Ta
D_z	...	≈ 6 nm
$\bar{d}$	$\approx 145\ \mu$m	$\approx 10\ \mu$m
j_{sw}	$\approx 10^9 - 10^{10}$ A/m^2	$\approx 10^{11}$ A/m^2
j_{dep}	$\approx 10^{10}$ A/m^2	$\approx 10^{11}$ A/m^2
Δ_{dep}	≈ 27	≈ 105

ACKNOWLEDGMENTS

We thank G. Reiss for making the laboratory equipment available. This work was partially supported by the Deutsche Forschungsgemeinschaft under sign ME 4389/2-1.

[1] I. M. Miron, K. Garello, G. Gaudin, P.-J. Zermatten, M. V. Costache, S. Auffret, S. Bandiera, B. Rodmacq, A. Schuhl, and P. Gambardella, Perpendicular switching of a single ferromagnetic layer induced by in-plane current injection, Nature **476**, 189 (2011).

[2] C. O. Avci, K. Garello, I. M. Miron, G. Gaudin, S. Auffret, O. Boulle, and P. Gambardella, Magnetization switching of an MgO/Co/Pt layer by in-plane current injection, Appl. Phys. Lett. **100**, 212404 (2012).

[3] A. Thiaville, S. Rohart, É. Jué, V. Cros, and A. Fert, Dynamics of Dzyaloshinskii domain walls in ultrathin magnetic films, Europhys. Lett. **100**, 57002 (2012).

[4] L. Liu, O. J. Lee, T. J. Gudmundsen, D. C. Ralph, and R. A. Buhrman, Current-Induced Switching of Perpendicularly Magnetized Magnetic Layers Using Spin Torque from the Spin Hall Effect, Phys. Rev. Lett. **109**, 096602 (2012).

[5] C.-F. Pai, L. Liu, Y. Li, H. W. Tseng, D. C. Ralph, and R. A. Buhrman, Spin transfer torque devices utilizing the giant spin Hall effect of tungsten, Appl. Phys. Lett. **101**, 122404 (2012).

[6] P. P. J. Haazen, E. Murè, J. H. Franken, R. Lavrijsen, H. J. M. Swagten, and B. Koopmans, Domain wall depinning governed by the spin Hall effect, Nat. Mater. **12**, 299 (2013).

[7] E. Martinez, S. Emori, and G. S. D. Beach, Current-driven domain wall motion along high perpendicular anisotropy multilayers: The role of the Rashba field, the spin Hall effect, and the Dzyaloshinskii-Moriya interaction, Appl. Phys. Lett. **103**, 072406 (2013).

[8] C. Zhang, M. Yamanouchi, H. Sato, S. Fukami, S. Ikeda, F. Matsukura, and H. Ohno, Magnetization reversal induced by in-plane current in Ta/CoFeB/MgO structures with perpendicular magnetic easy axis, J. Appl. Phys. **115**, 17C714 (2014).

[9] M. Cubukcu, O. Boulle, M. Drouard, K. Garello, C. O. Avci, I. M. Miron, J. Langer, B. Ocker, P. Gambardella, and G. Gaudin, Spin-orbit torque magnetization switching of a three-terminal perpendicular magnetic tunnel junction, Appl. Phys. Lett. **104**, 042406 (2014).

[10] K. Garello, C. O. Avci, I. M. Miron, M. Baumgartner, A. Ghosh, S. Auffret, O. Boulle, G. Gaudin, and P. Gambardella, Ultrafast magnetization switching by spin-orbit torques, Appl. Phys. Lett. **105**, 212402 (2014).

[11] R. Lo Conte, A. Hrabec, A. P. Mihai, T. Schulz, S.-J. Noh, C. H. Marrows, T. A. Moore, and M. Kläui, Spin-orbit torque-driven magnetization switching and thermal effects studied in Ta/CoFeB/MgO nanowires, Appl. Phys. Lett. **105**, 122404 (2014).

[12] G. Yu, P. Upadhyaya, K. L. Wong, W. Jiang, J. G. Alzate, J. Tang, P. K. Amiri, and K. L. Wang, Magnetization switching through spin-Hall-effect-induced chiral domain wall propagation, Phys. Rev. B **89**, 104421 (2014).

[13] Q. Hao and G. Xiao, Giant Spin Hall Effect and Switching Induced by Spin-Transfer Torque in a $W/Co_{40}Fe_{40}B_{20}/MgO$ Structure with Perpendicular Magnetic Anisotropy, Phys. Rev. Appl. **3**, 034009 (2015).

[14] G. Prenat, K. Jabeur, P. Vanhauwaert, G. D. Pendina, F. Oboril, R. Bishnoi, M. Ebrahimi, N. Lamard, O. Boulle, K. Garello, J. Langer, B. Ocker, M. C. Cyrille, P. Gambardella, M. Tahoori, and G. Gaudin, Ultra-fast and high-reliability SOT-MRAM: From cache replacement to normally-off computing, IEEE Trans. Multi-Scale Comput. Syst. **2**, 49 (2016).

[15] L. Neumann, D. Meier, J. Schmalhorst, K. Rott, G. Reiss, and M. Meinert, Temperature dependence of the spin Hall angle and switching current in the nc-W (O)/CoFeB/MgO system with perpendicular magnetic anisotropy, Appl. Phys. Lett. **109**, 142405 (2016).

[16] O. J. Lee, L. Q. Liu, C. F. Pai, Y. Li, H. W. Tseng, P. G. Gowtham, J. P. Park, D. C. Ralph, and R. A. Buhrman, Central role of domain wall depinning for perpendicular magnetization switching driven by spin torque from the spin Hall effect, Phys. Rev. B **89**, 024418 (2014).

[17] J.-V. Kim and M.-W. Yoo, Current-driven skyrmion dynamics in disordered films, Appl. Phys. Lett. **110**, 132404 (2017).

[18] S. Jaiswal, K. Litzius, I. Lemesh, F. Büttner, S. Finizio, J. Raabe, M. Weigand, K. Lee, J. Langer, B. Ocker, G. Jakob, G. S. D. Beach, and M. Kläui, Investigation of the Dzyaloshinskii-Moriya interaction and room temperature skyrmions in W/CoFeB/MgO thin films and microwires, Appl. Phys. Lett. **111**, 022409 (2017).

[19] W. Legrand, D. Maccariello, N. Reyren, K. Garcia, C. Moutafis, C. Moreau-Luchaire, S. Collin, K. Bouzehouane, V. Cros, and A. Fert, Room-temperature current-induced generation and motion of sub-100 nm skyrmions, Nano Lett. **17**, 2703 (2017).

[20] K. Fritz, S. Wimmer, H. Ebert, and M. Meinert, Large spin Hall effect in an amorphous binary alloy, Phys. Rev. B **98**, 094433 (2018).

[21] A. Hubert and R. Schäfer, *Magnetic Domains: The Analysis of Magnetic Microstructures* (Springer, Berlin, 2000).

[22] J. McCord, Progress in magnetic domain observation by advanced magneto-optical microscopy, J. Phys. D: Appl. Phys. **48**, 333001 (2015).

[23] M. Guizar-Sicairos, S. T. Thurman, and J. R. Fienup, Efficient subpixel image registration algorithms, Opt. Lett. **33**, 156 (2008).

[24] K. Zhang, W. Zuo, and L. Zhang, FFDNet: Toward a fast and flexible solution for CNN-based image denoising, IEEE Trans. Image Process. **27**, 4608 (2018).

[25] M. Tassano, J. Delon, and T. Veit, An analysis and implementation of the FFDNET image denoising method, Image Process. Line **9**, 1 (2019).

[26] L. Neumann and M. Meinert, Influence of the Hall-bar geometry on harmonic Hall voltage measurements of spin-orbit torques, AIP Adv. **8**, 095320 (2018).

[27] M. Hayashi, J. Kim, M. Yamanouchi, and H. Ohno, Quantitative characterization of the spin-orbit torque using harmonic Hall voltage measurements, Phys. Rev. B **89**, 144425 (2014).

[28] A. Jiang, T. A. Tyson, L. Axe, L. Gladczuk, M. Sosnowski, and P. Cote, The structure and stability of β-Ta thin films, Thin Solid Films **479**, 166 (2005).

[29] H. Li, G. Wang, D. Li, P. Hu, W. Zhou, S. Dang, X. Ma, T. Dai, S. Kang, F. Yu, X. Zhou, S. Wu, and S. Li, Field-free deterministic magnetization switching with ultralow current density in epitaxial Au/Fe_4N bilayer films, ACS Appl. Mater. Interfaces **11**, 16965 (2019).

[30] C.-Y. You, I. M. Sung, and B.-K. Joe, Analytic expression for the temperature of the current-heated nanowire for the current-induced domain wall motion, Appl. Phys. Lett. **89**, 222513 (2006).

[31] R. H. Koch, J. A. Katine, and J. Z. Sun, Time-Resolved Reversal of Spin-Transfer Switching in a Nanomagnet, Phys. Rev. Lett. **92**, 088302 (2004).

[32] V. Jeudy, A. Mougin, S. Bustingorry, W. Savero Torres, J. Gorchon, A. B. Kolton, A. Lemaître, and J. P. Jamet, Universal Pinning Energy Barrier for Driven Domain Walls in Thin Ferromagnetic Films, Phys. Rev. Lett. **117**, 057201 (2016).

[33] R. Diaz Pardo, W. Savero Torres, A. B. Kolton, S. Bustingorry, and V. Jeudy, Universal depinning transition of domain walls in ultrathin ferromagnets, Phys. Rev. B **95**, 184434 (2017).

[34] V. Jeudy, R. Díaz Pardo, W. Savero Torres, S. Bustingorry, and A. B. Kolton, Pinning of domain walls in thin ferromagnetic films, Phys. Rev. B **98**, 054406 (2018).

[35] A. V. Khvalkovskiy, D. Apalkov, S. Watts, R. Chepulskii, R. S. Beach, A. Ong, X. Tang, A. Driskill-Smith, W. H. Butler, P. B. Visscher, D. Lottis, E. Chen, V. Nikitin, and M. Krounbi, Basic principles of STT-MRAM cell operation in memory arrays, J. Phys. D: Appl. Phys. **46**, 074001 (2013).

[36] J. H. Franken, M. Herps, H. J. M. Swagten, and B. Koopmans, Tunable chiral spin texture in magnetic domain-walls, Sci. Rep. **4**, 5248 (2015).

[37] R. Soucaille, M. Belmeguenai, J. Torrejon, J.-V. Kim, T. Devolder, Y. Roussigné, S. M. Chérif, A. A. Stashkevich, M. Hayashi, and J.-P. Adam, Probing the Dzyaloshinskii-Moriya interaction in CoFeB ultrathin films using domain

wall creep and Brillouin light spectroscopy, Phys. Rev. B **94**, 104431 (2016).

[38] M. Vaňatka, J. C. Rojas-Sánchez, J. Vogel, M. Bonfim, M. Belmeguenai, Y. Roussigné, A. Stashkevich, A. Thiaville, and S. Pizzini, Velocity asymmetry of Dzyaloshinskii domain walls in the creep and flow regimes, J. Phys.: Condens. Matter **27**, 326002 (2015).

[39] A. K. Chaurasiya, C. Banerjee, S. Pan, S. Sahoo, S. Choudhury, J. Sinha, and A. Barman, Direct observation of interfacial Dzyaloshinskii-Moriya interaction from asymmetric spin-wave propagation in W/CoFeB/SiO_2 heterostructures down to sub-nanometer CoFeB thickness, Sci. Rep. **6**, 32592 (2016).

[40] J. Prommier, P. Meyer, G. Pénissard, J. Ferré, P. Bruno, and D. Renard, Magnetization Reversal in Ultrathin Ferromagnetic Films with Perpendicular Anistropy: Domain Observations, Phys. Rev. Lett. **65**, 2054 (1990).

[41] K.-J. Kim, R. Hiramatsu, T. Moriyama, H. Tanigawa, T. Suzuki, E. Kariyada, and T. Ono, Tradeoff between low-power operation and thermal stability in magnetic domain-wall-motion devices driven by spin Hall torque, Appl. Phys. Express **7**, 53003 (2014).